Research Article | Vol. 31, No. 24 / 20 Nov 2023 / Optics Express 40687
Optics EXPRESS

Detrimental effects of period-chirped gratings in pulse compressors

FLORIAN BIENERT,* CHRISTOPH RÖCKER, TOM DIETRICH, THOMAS GRAF, AND MARWAN ABDOU AHMED

Universität Stuttgart, Institut für Strahlwerkzeuge (IFSW), Pfaffenwaldring 43, 70569 Stuttgart, Germany
florian.bienert@ifsw.uni-stuttgart.de

Abstract: We present a comprehensive simulative and experimental investigation of how period-chirped pulse compression gratings affect the compressed pulses. A specifically developed ray-tracing tool was used for the simulative investigations. It is shown that the chirp creates a characteristic spatio-spectral error pattern, which leads to a degradation of the beam quality and an increase of the pulse duration. The experimental investigations, for which both a narrow-bandwidth continuous-wave and a pulsed laser beam were guided through a Treacy-compressor comprised of period-chirped gratings, confirm the simulation results and present methods on how to identify the chirp's characteristic error pattern in practice.

1. Introduction

Almost 40 years after the invention of chirped-pulse amplification (CPA) by Gérard Mourou and Donna Strickland [1] pulse compressors and stretchers are commonly used in laser amplifier systems [2–5]. Today, their application enables the generation of pulses with peak powers up to the order of petawatts [6] and might pave the way to reach the exawatt level [7]. Although various pulse compressor architectures are known [8–11], especially grating-based compressors are popular as they are suitable to provide high group delay dispersion (GDD) and since they can withstand high pulse energies. Used in the classic Treacy configuration [12], only two gratings and two mirrors are required. When aiming at the compression of broadband pulses close to the Fourier limit with high beam quality, the alignment and the precise fabrication of the components become crucial [13,14]. For this reason, both misalignment [15,16] and surface deformations of the gratings, originating from their fabrication [17,18], thermal load [19–21], or mechanical stress [22,23] were the subjects of intense research. Besides the implementation of complex simulations [24], even techniques for the pre-compensation of the gratings's wavefront errors have been reported [25]. Typical spatio-temporal aberrations arising from such errors are the tilt of the pulse front, spatial chirp, angular chirp, and an increased pulse duration [17,18,26–29]. These undesirable detrimental effects indicate the necessity of precisely manufactured gratings with high optical quality.

Techniques that are commonly used for the fabrication of linear gratings are nanoimprint lithography [30], electron-beam lithography [31], scanning beam interference lithography (SBIL) [32,33], or classical laser interference lithography (LIL) [34–36]. Due to its simple implementation, its inexpensive use [37,38], and the possibility to enable the one-shot exposure of large gratings [35] LIL is a popular technique for the fabrication of linear gratings. In contrast to the other above listed techniques LIL is however accompanied by the detrimental effect of period chirp [39,40]. It is a consequence of the finite curvature of the wavefronts of the interfering laser beams used for the exposure of the photoresist to create the grating lines. For the commonly used lithographic setups, the period chirp has two aspects [41–43]. The first is a spatial dependence of the period on the substrate, which increases approximately quadratically from the center of

#505875 https://doi.org/10.1364/OE.505875
Journal © 2023 Received 19 Sep 2023; revised 2 Nov 2023; accepted 4 Nov 2023; published 15 Nov 2023

Optics EXPRESS

the interference pattern toward the edges. Related to this first effect, the second is a spatially dependent inclination of the grating lines [43,44] that also increases from the center of the interference pattern towards the edges. Details on this can be found in [43,44] and are visualized later in the text in Fig. 2. The magnitude of the chirp is highly dependent on the implementation of the lithographic setup. When a proper collimation is applied to the interfering beams [34] the period chirp can be minor [43]. To reduce the costs and avoid possible phase distortions from the collimating optics, the use of divergent beams is however also quite common. For such setups, the magnitude of the chirp of the gratings scales quadratically with a decreasing distance between the point sources and the substrate. Typical distances used by grating suppliers (including the supplier of the gratings shown in this work) range within a few meters, but also one meter [42] or even less [45–47] can be found in the literature, thus leading to a very strong chirp. Although the chirp is a known problem, its impact on the performance of optical systems has barely been investigated yet.

Especially when employing gratings manufactured by LIL in pulse compressors, we expect the influence on the pulses to be critical since these systems are known to be exceptionally sensitive and since these systems employ large gratings. However, despite the extensive use of both grating-based pulse compressors and gratings fabricated by LIL, the influence that the period chirp has on the performance of pulse compressors has not been addressed so far.

With the present contribution, we, therefore, report on the impact that the period chirp of pulse compression gratings has on the compressed laser pulses. In the first part, the setup and the gratings are discussed in detail. In the second part (section 3), ray-tracing simulations are reported on, that were performed to quantitatively investigate the influence of the period chirp on the pulses that are compressed in a classical Treacy configuration [12]. The third part (section 4) is devoted to experiments using the compressor presented in the first part. The first experiment was performed to determine the detrimental effects that the period chirps of the gratings have on the compressed beam (section 4.1). In a second and third experiment both a pulsed laser beam and a continuous-wave (cw) beam were guided through the pulse compressor (sections 4.2 and 4.3) to validate the simulation and to illustrate experimental methods that are suitable to identify the pulse aberrations caused by the period chirp in a hands-on manner.

2. Setup

The compressor considered in the present report is schematically shown in Fig. 1. It consists of two gratings and a retroreflector (RR) set up in the classical Treacy configuration [12]. Both gratings had a size of 75 mm × 50 mm, a nominal grating period of $\Lambda_0 = 610$ nm and experienced two passes of the beam, whose initial diameter was $d_B = 5$ mm, as shown in Fig. 1(a). The dispersion length of the compressor was $l_0 = 341$ mm, introducing a group delay dispersion of $GDD = -20$ ps^2 for the central wavelength of $\lambda_g = 1030$ nm. The distance between the center of the second grating (G2) and the RR was 250 mm. As depicted in Fig. 1(b), the angle of incidence (AOI) on the first grating (G1) was $\theta_{inc} = 51.4°$ while the angle of diffraction (AOD) of the – 1st diffraction order was $\theta_{-1}(\lambda_g) = -65.1°$ at the central wavelength.

The two used gratings had identical specifications and were fabricated by AMO GmbH using LIL for the exposure of the photoresist [48]. The period of these gratings was measured using the diffractometric setup that we presented in [49]. It is based on a modified long-trace profiler and enables a measurement accuracy of 15 pm for these gratings. Figure 2(a) shows the spatially resolved measurement of the grating period of one of the two gratings. The other one was found to have identical properties.

The chirp, i.e. the parabolic increase of the period with increasing distance from the center of the substrate is clearly visible, indicated by both the color scale and the vertical axis. The data shows that the chirp measured along the y-direction (parallel to the grating lines, $||$) is much smaller than the chirp observed along the x-direction (perpendicular to the grating lines, $\perp$). This

Optics EXPRESS

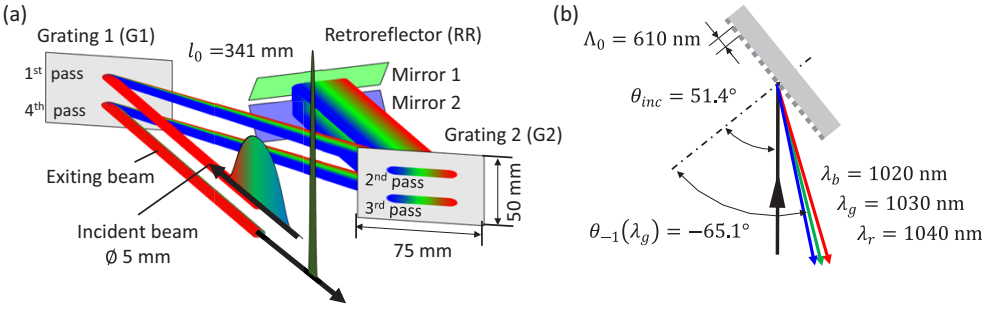

Fig. 1. (a): Setup of the considered compressor. The coloring of the beam indicates the longer (red) and shorter (blue) wavelengths with respect to the central wavelength (green). (b): Angle of incidence θ_{inc}, angle of diffraction θ_{-1}, and nominal grating period Λ_0 of the first grating.

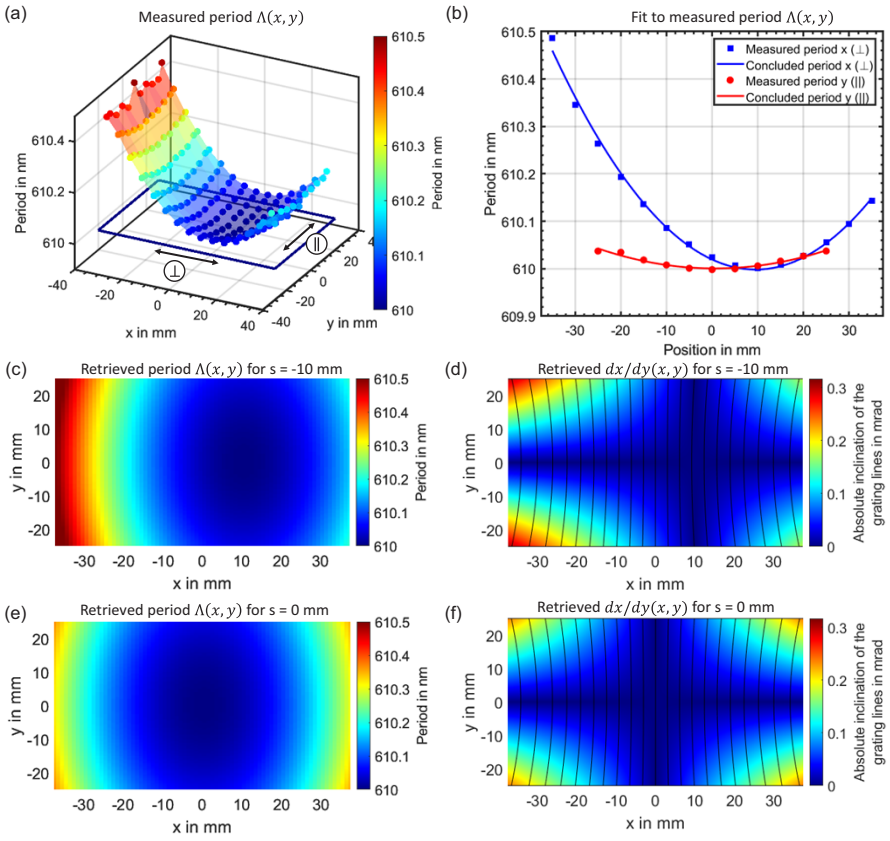

Fig. 2. (a): Measured spatial distribution of the period $\Lambda(x,y)$ of the gratings from [49]. (b): Measured and fitted grating period at the center of the substrate perpendicular to the grating lines $\Lambda(x, 0$ mm) (blue) and parallel to the grating lines $\Lambda(x = 0$ mm,$y)$ (red). (c): Calculated $\Lambda(x,y)$ for parameters retrieved from the measurements. (d): Calculated $dx/dy(x,y)$ for parameters retrieved from the measurements. The inclination of the grating lines (black) is strongly exaggerated for visibility. (e): Calculated $\Lambda(x,y)$ of a grating assuming an ideally centered chirp. (f): Calculated $dx/dy(x,y)$ of a grating assuming an ideally centered chirp.

Optics EXPRESS

is emphasized by the corresponding results evaluated along the x-axis in the center of the substrate at $y = 0$ mm (blue squares) and in the y-direction at $x = 0$ mm (red dots) shown in Fig. 2(b). The minimum of the grating period (vertex of the parabola) is displaced off the substrate's center by approximately +10 mm in the x-direction and by – 0.5 mm in the y-direction. This displacement is attributed to a mispositioning of the substrate with respect to the center of the interference pattern that was used for the exposure. While the chirp, i.e the parabolic increase of the period, is an intrinsic consequence of the lithographic approach LIL [44] and commonly observed for LIL gratings, the displacement of the parabolic distribution is an error, specific to the supplier's implementation of LIL. The small displacement of the distribution of the grating period in the y-direction is negligible and therefore not further considered in the following. The blue and red curves shown in Fig. 2(b) are parabolic fits to the measured data. Using the coefficients of these fits the spatial function of the period is determined to

$$\Lambda(x,y) = 0.222 \cdot \frac{pm}{mm^2} \cdot (x+s)^2 + 0.077 \cdot \frac{pm}{mm^2} \cdot y^2 + 610nm. \tag{1}$$

The parameter $s = -10$ mm accounts for the displacement of the vertex of the paraboloid from the center of the substrate for the present grating sample. Figure 2(c) shows the spatial function of the period calculated from Eq. (1).

The spatial function of the inclination of the grating lines $dx/dy(x,y)$ cannot be measured by means of our setup. The distribution $dx/dy(x,y)$ can however be calculated when the position of the point sources which were used to generate the interference pattern in the lithographic setup is known with respect to the position of the substrate [44]. Knowing the exposure wavelength of $\lambda_{exp} = 266$ nm given by the supplier, the arrangement that was used to manufacture our gratings was retrieved from the measured spatial distribution $\Lambda(x,y)$ as given in Eq. (1) by means of the model described in [44]. It was found that the two point sources were separated by $2 \cdot x_s$ with $x_s = 433$ mm in x-direction and that they were positioned at a perpendicular distance of $z_s = 1938$ mm from the substrate's surface [44]. Using this information, the spatial distribution of the inclination of the grating lines $dx/dy(x,y)$ can be calculated with Eq. (34) from [44]. Taking into account the observed displacement by the amount of s in the x-direction between the interference pattern and our substrates within the lithographic processing, the spatial distribution of the inclination of the grating lines on our samples is found to be

$$\frac{dx}{dy}(x,y) = \frac{(x+s)^2 \cdot y \cdot \sqrt{z_S^2 + y^2 + x_S^2 + (x+s)^2}}{\sqrt{((x+s)^2 z_S^2 + (x+s)^2 y^2 + (x_S^2 + y^2 + z_S^2)^2)(x_S^2 + y^2 + z_S^2)}} \tag{2}$$

Figure 2(d) shows the spatial distribution of the inclination of the grating lines $dx/dy(x,y)$ calculated with Eq. (1) for $s = -10$ mm. The black lines illustrate the inclination of the grating lines, but are strongly exaggerated for visibility.

Due to the eccentric chirp of our gratings, their orientation (upright or upside-down) when mounted in the compressor is of high importance because it determines the position of the vertex of the spatial functions of the period and the inclination of the grating lines with respect to the laser beam. The upright and upside-down orientation of the gratings were investigated both in the simulation and in the experiments as reported below. Since the eccentric chirp of our gratings was not planned, but is a consequence of an error in the manufacturing, the results that can be expected when the chirp is assumed to be centered on the gratings but with the same magnitude as described above were also investigated with the simulation. Hence, the spatial function of the period $\Lambda(x,y)$ and the inclination of the grating lines $dx/dy(x,y)$ of this assumed grating were calculated from Eq. (1) and Eq. (2) with $s = 0$ mm. The resulting spatial functions of the period and the inclination of the grating lines are shown in Fig. 2(e) and (f).

Optics EXPRESS

3. Analysis based on simulations

To allow for a precise and comprehensive simulation of the propagation of pulses through a grating compressor comprising chirped gratings (taking into account both the spatially dependent period and the inclination of the grating lines) we developed a ray tracer specifically for this task. For its implementation, the beam is modelled by 11 ray bundles, each consisting of 25 rays. While all rays within one bundle have the same wavelength, different bundles (and the included rays respectively) have different wavelengths evenly spaced by 2 nm, from $\lambda_b = 1020$ nm to $\lambda_r = 1040$ nm. All bundles are exactly superposed in space thus representing the spectral composition of the propagating pulses. The 25 rays of each bundle are used to model the diameter and divergence of each of the beam's different spectral components. Each ray is described as a line in space defined with an origin, direction, wavelength, intensity, and phase. In Fig. 3 the intersection between one bundle and a plane is depicted, showing the arrangement of the 25 rays within the bundle. All rays originate at the same point (point source model). The central ray is located on the optical axis of the beam, 16 outer rays represent the beam's circumference defined by $1/e^2$ (this measure will also be used in the experiments in section 4) and 8 inner rays are added to increase the resolution of the beam in the simulation. The developed ray tracer takes into account the spatial distributions of the period $\Lambda(x,y)$ and the inclination of the grating lines $dx/dy(x,y)$ for the gratings, as well as a misalignment and surface deformations for all optical components.

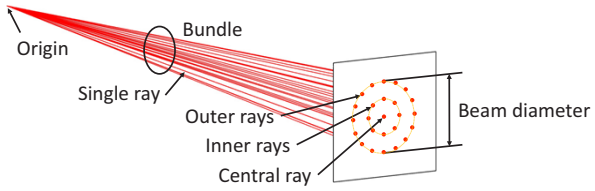

Fig. 3. In the simulation each spectral component of the laser beam is represented by a bundle of 25 rays.

Figure 4 shows the raytracing simulation of the beam propagation through a compressor comprised of perfectly aligned and ideally manufactured optical components (i.e. no chirp: $\Lambda(x,y) = 610$ nm and $dx/dy(x,y) = 0$). The diameter and the divergence of the incident beam were defined to be $d_B = 5$ mm and $\vartheta = 0.17$ mrad (assuming a beam with a beam propagation factor of $M^2 = 1.3$) at the position of the first grating G1. The spectral components of the incident beam are dispersed by the diffraction that occurs at the first interaction with the grating G1 and subsequently reach the surface of the grating G2, where the spatial separation of the 11 bundles representing the spectral components of the pulses (color coded) can be seen.

After being collimated by grating G2, reflected by the retroreflector RR, and after passing the setup for a second time, all spectral components collinearly overlap again when leaving the compressor. The properties of the beam exiting the compressor, i.e. the position, angle, and beam diameter of its 11 spectral components, are analyzed using the two planes labeled P1 and P2 in Fig. 4(a). Plane P1 is located in front of the lens L (at a distance of 210 mm from G1) and plane P2 is located in the lenses' focal plane behind the lens L. Hence plane P1 serves to identify any lateral shifts of the different spectral components while P2 is used to detect tilting of the different spectral components. The focal length of the lens is $f = 100$ mm. The analysis of the beam in these two planes enables a direct and intuitive comparison to the experimental results presented in section 4. Figure 4(b) shows the intersections of the 11 bundles representing the spectral components of the beam with the plane P1. Only the central ray and the outer 16 rays (see Fig. 3) representing the beam circumference (at $1/e^2$) of each spectral component are shown and connected to a ring for the sake of clarity. The slightly different widths (x-direction)

Optics EXPRESS

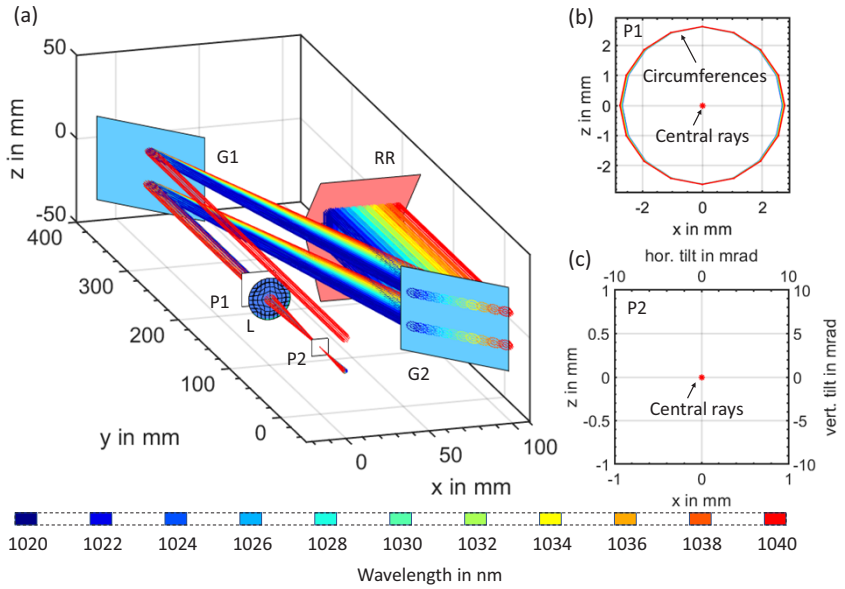

Fig. 4. Raytracing simulation of the beam propagation in a pulse compressor with ideal alignment and unchirped gratings. The properties of the compressor and the beam are the same as those already specified in Fig. 1. (a): Three-dimensional view of the beam propagating in the compressor. The exiting (compressed) beam is analyzed in the two planes P1 and P2. P1 is located in front and P2 behind (in the focal plane of) the lens L (f = 100 mm). (b): Central rays (optical axes) and circumferences (16 rays) of the cross sections of the 11 bundles representing the spectral components of the pulses at the location of plane P1. (c): Central rays (optical axes) of the 11 bundles representing the spectral components of the pulses at the location of plane P2. Due to the perfect overlap of the spectral components, only a single dot is seen in the figure.

of the beams of the different spectral components are a consequence of the divergence of the incident beam ($\vartheta = 0.17$ mrad) as shown by Heathcote et al. [50]. Figure 4(c) shows the position of the central rays of the 11 spectral components at the plane P2. The additional axes on the top and right side of the figure indicate the tilts of different spectral components in the vertical and horizontal direction when intersecting the lens L. The results show that when the compressor is perfectly aligned and comprised of unchirped gratings, as expected, all spectral components of the beam are coaxially superimposed after compression (with no lateral displacement as analyzed in P1 and no tilt as analyzed in P2).

The simulation of the beam propagation through a misaligned compressor but still with unchirped gratings is shown in Fig. 5, where the second grating G2 is rotated by 0.2° around the vertical axis.

As seen from Fig. 5(b) and (c) the spectral components are subject to different shifts and tilts after exiting the compressor. These two effects are more commonly known by the terms spatial chirp and angular chirp, respectively [13,51]. We will however avoid these terms to avoid confusion with the period chirp treated in the present paper.

For the following discussion, it is important to note that the shifts and tilts of the spectral components observed in Fig. 5, which are induced by the considered misalignment of G2, increase strictly monotonously with increasing wavelength. The same monotonous dependence of the shifts and tilts of the different spectral components on their wavelength was also observed for the misalignment (around all axes) of the other grating G1, and of the mirrors of the retroreflector

Optics EXPRESS

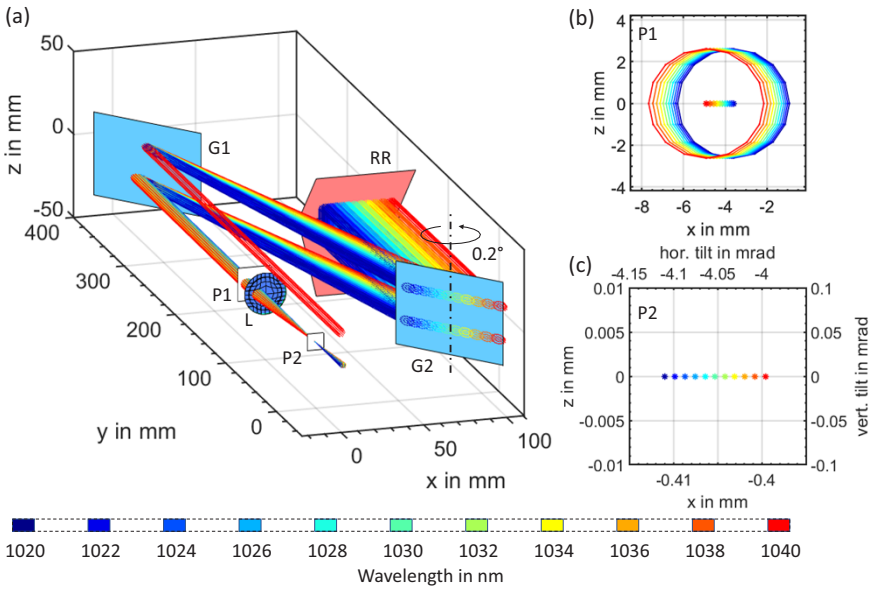

Fig. 5. Raytracing simulation of the beam propagation in a pulse compressor comprised of unchirped gratings but in which grating G2 is misaligned by 0.2°. The other properties of the compressor and the beam are the same as those already specified in Fig. 1. (a): Three-dimensional view of the beam propagating in the compressor. (b): Central rays (optical axes) and circumferences (16 rays) of the 11 bundles representing the spectral components of the pulses at the location of plane P1. (c): Central rays (optical axes) of the 11 bundles representing the spectral components of the pulses at the location of plane P2.

RR. This is consistent with the results presented in other publications [13,15,28]. In addition to misalignment, also spherical deformations of the surfaces of the different optics were investigated, which also consistently resulted in shifts and tilts of the different spectral components with a monotonous dependence on their wavelength.

Figure 6 shows the simulation of the beam propagation through an ideally aligned compressor where both gratings exhibit the same chirp as our sample but without a lateral displacement of the distributions with respect to the center of the element. The spatial distribution of the grating period $\Lambda(x,y)$ and of the inclination of the grating lines $dx/dy(x,y)$ are therefore given by the Eqs. (1) and (2), respectively, but with $s = 0$ mm. The results of the simulation depicted in Fig. 6(b) show that at the exit of the compressor, the beams of the red-shifted spectral components are horizontally stretched while the beams of the blue-shifted spectral components are spatially narrowed in the horizontal direction. This is not a consequence of the beam's collimation but arises from the period chirp. The central rays of the different spectral components are distributed along a c-shaped curve, where the blue-shifted spectral components are located on the top right ($x > 0$ mm $y > 0$ mm), the central spectral component is located on the left with no vertical displacement ($x = 0$ mm $y = 0$ mm), and the red-shifted spectral components are located on the lower right ($x > 0$ mm $y < 0$ mm). The same distribution of the central rays of the spectral components along a c-shaped curve can also be observed in the plane P2, depicted in Fig. 6(c), indicating the tilts of the spectral components.

It is seen from Fig. 6(b) and (c) that the spectral components are shifted and tilted in the vertical axis with a monotonous dependence on their wavelength (i.e. blue-shifted spectral components are located above the central spectral component and red-shifted spectral components are located below the central component), while in the horizontal axis, both red- and blue-shifted spectral

Optics EXPRESS

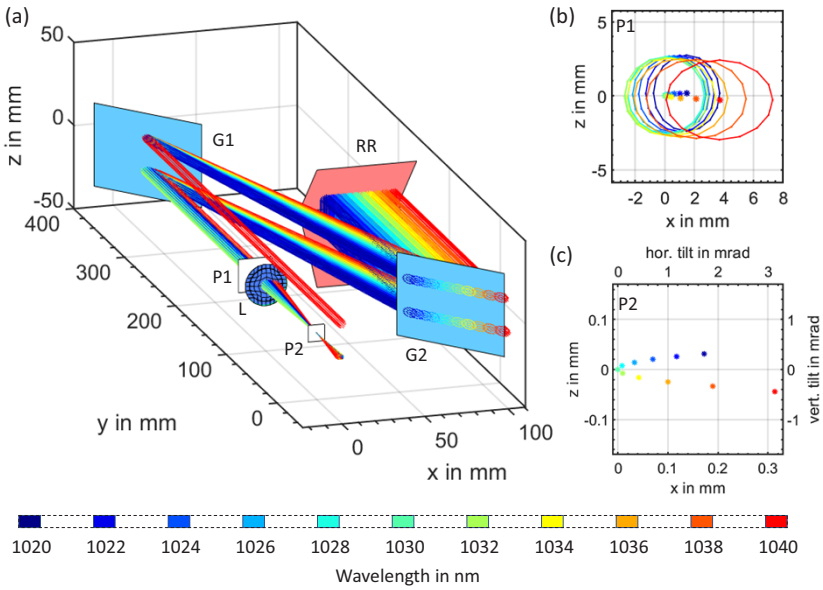

Fig. 6. Raytracing simulation of the beam propagation in a perfectly aligned pulse compressor, comprising gratings with a centered chirp, see Fig. 2. The other properties of the compressor and the beam are the same as those already specified in Fig. 1. (a): Three-dimensional view of the beam propagating in the compressor. (b): Central rays (optical axes) and circumferences (16 rays) of the 11 bundles representing the spectral components of the pulses at the location of plane P1. (c): Central rays (optical axes) of the 11 bundles representing the spectral components of the pulses at the location of plane P2.

components are shifted and tilted towards the same side, i.e. to the right. Furthermore, it is noticeable that the central spectral component exits the compressor without being shifted or tilted. Thereby the observed effects on the spectral components in the horizontal direction are a consequence of the spatially dependent period, while the effects on the spectral components in the vertical direction are a consequence of the spatially dependent inclination of the grating lines. It introduces an additional tilt of the diffracted beams out of the *xy*-plane and thus breaks the vertical symmetry of the setup.

This spatio-spectral error pattern observed in Fig. 6 is unique for the period chirp. We also simulated other, more commonly observed effects in compressors, such as the misalignment of the different optical components and their spherical deformation. However, even when they were combined in different permutations, they could not reproduce a similar pattern.

The simulation shown in Fig. 6 assumed that the spatial distribution of the chirp was centred on the grating elements. The results obtained by also considering the acentric position of the chirp as given by the Eqs. (1) and (2) with $s = -10$ mm (upright orientation of the sample) and $s = 10$ mm (upside-down orientation of the sample) are shown in Fig. 7 and compared to the previously discussed performance of the compressor with $s = 0$ mm (see Fig. 6(b) and (c)). According to Fig. 7(a), the spectral components in the plane P1 are distributed along a similar c-shaped curve in all three cases. The red-shifted spectral components however experience stronger shifts when both gratings are orientated upright, while the blue-shifted spectral components experience stronger shifts when both gratings are orientated upside-down. The same characteristic pattern can also be observed with regard to the tilt as seen from the distribution of the central rays in the plane P2, depicted in Fig. 7(b). Additional simulations showed that the permutation of the arrangement of the two gratings (i.e. one upright and the other upside-down) leads to a similar

Optics EXPRESS

distribution of the shift and tilts of the spectral components. This can be seen exemplarily from the last curve in Fig. 7(b) where the first grating was arranged in upright and the second grating was arranged in upside-down orientation. The same behavior could be observed for the shifts, but the corresponding curve is not inserted in the figure (Fig. 7(a)) for the sake of clarity.

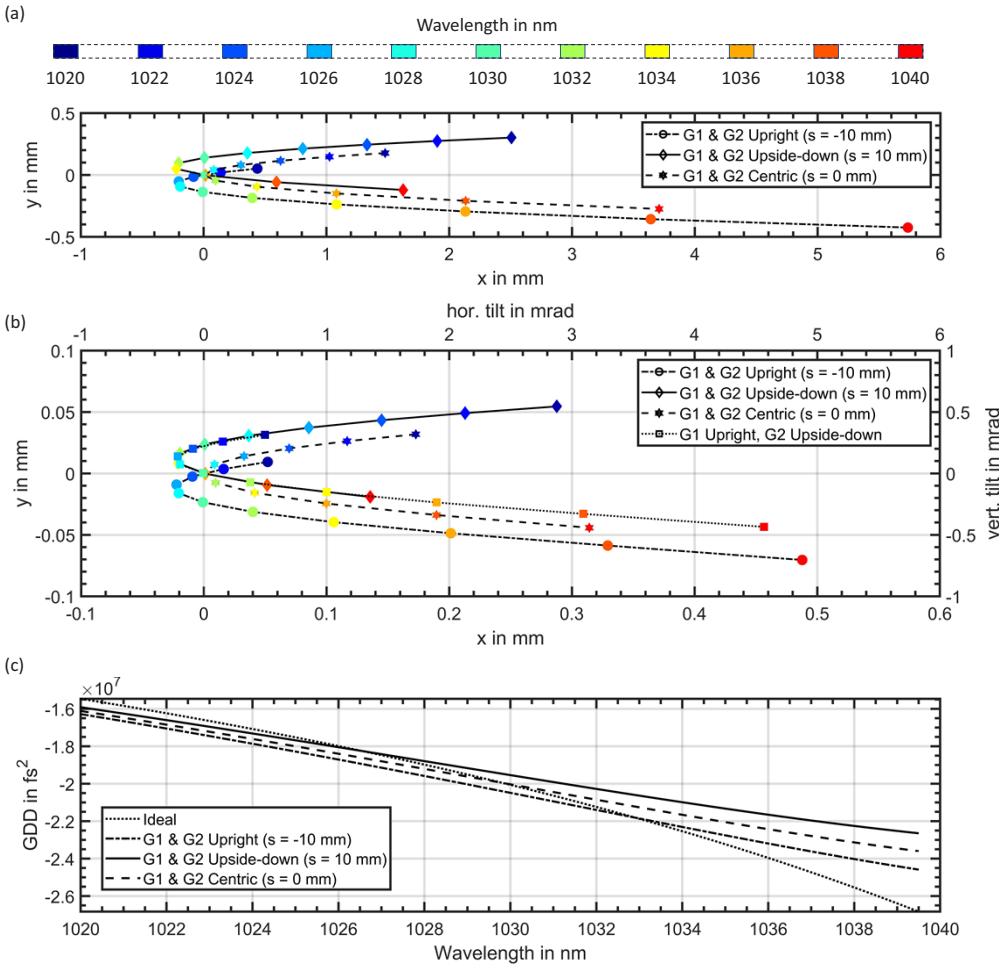

Fig. 7. Simulated influence of the lateral displacement s of the chirp (with respect to the center of the gratings) on the beam exiting the compressor. (a): Shifts of the spectral components at the plane P1 visualized by the position of their central rays. (b): Tilts of the spectral components represented by the location of their central rays at the plane P2. (c): Simulated group delay dispersion (GDD) for an ideal compressor with unchirped gratings and compressors comprising gratings with the chirp as measured on our sample with different lateral displacements s.

Both the observed shifts and tilts of the spectral components result in a non-collinear superposition of the spectral components of the compressed pulses and are therefore expected to reduce the beam quality of the beam exiting the compressor. The simulations showed that the period chirp of the gratings also affects the dispersion of the compressor, which is important for the temporal properties of the compressed pulses [2,52]. This is exemplarily shown for the group delay dispersion (GDD) of the compressor in Fig. 7(c). For comparison, the GDD of the compressor with un-chirped gratings is added (dotted line). The comparison of the results shows

Optics EXPRESS

that the influence of the chirp on the GDD is stronger on the red-shifted side of the spectrum. Assuming that the GDD of the compressor with un-chirped gratings (dotted line) leads to an ideal fourier-transform-limited duration of the compressed pulses, an increase of the pulse duration and a change in the temporal pulse shape can be expected for the pulses which are compressed by compressors equipped with chirped gratings. The quantitative changes in pulse duration, as well as in beam quality however ultimately depend on the shape of the pulse's spectral intensity.

4. Experimental investigation

Three different experiments were conducted with the compressor that is schematically shown in Fig. 1, using the period-chirped gratings in upright orientation ($s = -10$ mm), as shown in Fig. 2(c) and (d). In the first experiment, the beam of a pulsed laser was guided through the compressor to demonstrate the detrimental influence of the period chirp on the beam quality and the duration of the compressed pulses. For the second experiment, the same pulsed laser was used to qualitatively investigate the tilt of the individual spectral components exiting the compressor. In the third experiment, a wavelength-tunable continuous-wave (cw) laser was used to quantitatively measure the shifts of the individual spectral components exiting the compressor over a broad spectral range.

For all three experiments, a collimated beam was used and the compressor was set up as shown in Fig. 1 to match the simulation as closely as possible. The alignment of the compressor was carried out according to the procedure presented by Miesak et al. [53].

4.1. Effects of the period chirp on the compressed pulses

In order to measure the influence of the period chirp on the beam quality and the duration of the compressed pulses, the setup depicted in Fig. 8(a) was used. Temporally stretched pulses with a duration of $\tau = 90$ ps and a repetition rate of 1 MHz were injected into the compressor. Although the maximum available average power of the laser was 1 kW [54], only low power (1 W) was used for the experiments to exclude any thermal effects [19,20]. The spectrum of the injected pulses is shown in Fig. 8(b). The beam propagation factors of both the injected and the compressed beam were measured using the beam analysis device Ophir-Spiricon M2-200.

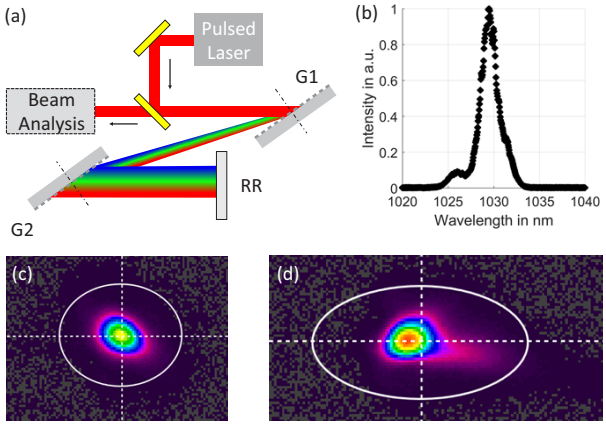

Fig. 8. (a): Sketch of the setup for the investigation of the effects of the period chirp on the beam propagation factor of the compressed beam and the duration of the compressed pulses. (b): Spectral intensity distribution of the incident laser pulses before injection into the compressor. (c): Intensity distribution of the beam in the focal plane of the beam analysis device before passing the compressor (d): Intensity distribution of the beam in the focal plane of the beam analysis device after passing the compressor.

Optics EXPRESS

Figure 8(c) and (d) show the obtained intensity distributions of the beam in the focal plane of the lens of the beam analysis device before (c) and after (d) passing the pulse compressor. The injected beam shows a rather round and homogenous intensity distribution and beam propagation factors of $M^2_x = 1.4$ and $M^2_y = 1.3$ in the horizontal and vertical axis, respectively, were measured. As seen from Fig. 8(d), the intensity distribution of the compressed beam shows a tail on the right-hand side causing a degradation of the beam propagation factors to $M^2_x = 2.76$ and $M^2_y = 1.6$. Both the stronger degradation of the beam quality in the x-direction and the elongation of the beam's intensity distribution toward the lower right side are consistent with the results from the simulation, see Fig. 7(b). In order to measure the pulse duration of the beam, a partially reflective mirror was used to generate a low-power replica of the beam at full aperture. By means of an autocorrelator from APE GmbH (based on second harmonic generation), a pulse duration was measured to be $\tau = 900$ fs (sech^2). With respect to a pulse duration of $\tau = 570$ fs (sech^2) expected from an ideal compression, the pulses hence show a strong temporal elongation. This increase in the duration is expected from the results of the simulation, see Fig. 7(c).

4.2. Measuring the chirp-induced tilt with a pulsed laser

That the period chirp of the gratings is the reason for the observed degradation of the beam quality is seen by investigating the tilt of the individual spectral components in the compressor's exiting beam. For this purpose, the experimental setup was modified as shown in Fig. 9(a). At reduced incident power (100 mW), the beam exiting the compressor was again analyzed by the Ophir-Spiricon M2-200. While recording the beam's intensity distribution in the focal plane of the analyzing device, a knife edge was moved slowly into the beam path between grating G2 and the retroreflector RR, as shown in Fig. 9(a). Due to the spatial separation of the pulse's spectral components between G2 and the RR, they are cut off by the knife edge and thus disappear in the intensity distribution at the focus of the beam. The wavelengths of the spectral components seen at different positions in the focal plane was identified by exploiting that according to the simulations there is an approximately linear relation between the location of the knife edge and the wavelengths that are cut off. Knowing the spectrum of the pulses as depicted in Fig. 8(b) it was therefore possible to approximately (with an accuracy of ±1 nm) assign the wavelengths of the spectral components seen at different locations in the images recorded in the focal plane of the analyzing device. This correlation is illustrated in Fig. 9(b), where six exemplary recordings of the beam's intensity distribution are shown for different positions of the knife edge. The denoted wavelength range corresponds to the spectral range that is not cut off by the knife edge. The full recording of the beam's intensity distribution with the camera can be found as a video in the supplementary material of this publication (see Visualization 1). The exposure time of the camera was set to obtain an oversaturated image to detect even low-intensity spectral components far from the center of gravity of the beam's intensity profile, which showed strong distortions. Figure 9(c) shows the final results of this analysis, disclosing the location of the different spectral components within the beam's focal plane.

The results from Fig. 9(c) show that the red-shifted spectral components are stretched and located at the lower right side of the intensity profile. Slightly blue-shifted spectral components are located at the left side while the strongly blue-shifted spectral components are shrunk and located at the upper right side of the intensity profile. This observation of the location of the beam's spectral components in the beam's focal plane corresponds to the method presented in our simulation using the lens L and plane P2 (see Fig. 6), hence indicating tilts of the spectral components within the beam. The experimental results can therefore directly be compared to the simulation's results depicted Fig. 7(b) where the locations of the spectral components in the beam's focal plane for the upright orientation of the chirped gratings are depicted. The comparison reveals a high agreement between the simulation and the experiments. Any minor deviations between the simulative prediction and the experimental observations (i.e. the shape of

Optics EXPRESS

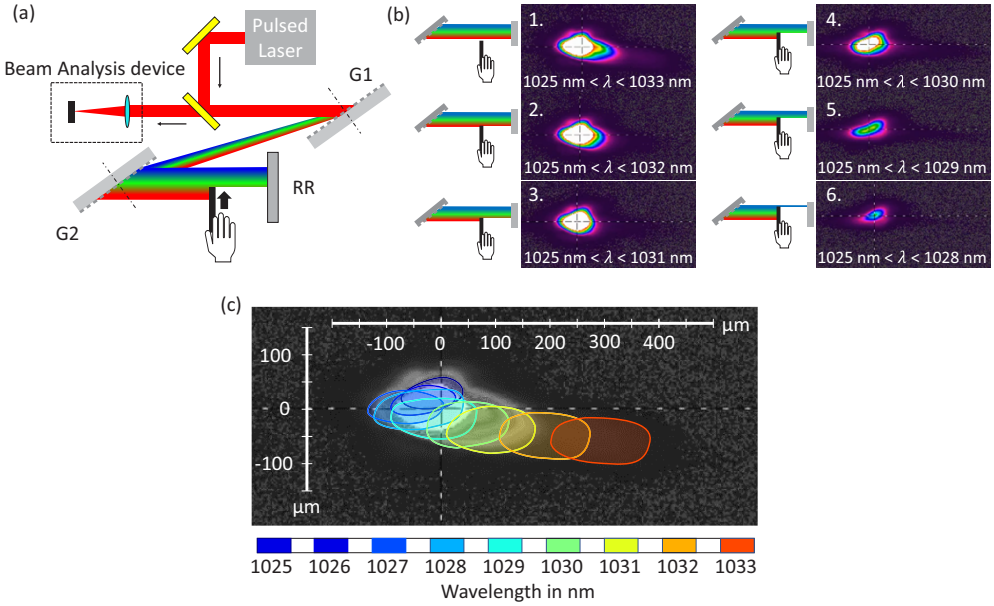

Fig. 9. Sketch showing a method to identify the chirp as the cause for the observed degradation of the beam quality. A knife edge is introduced between G2 and the RR to cut off spectral components while the beam's intensity profile is observed at the focus of the beam analyzer. (a): Simplified sketch of the optical setup. (b): Beam profiles and their spectral composition (with an accuracy of ±1 nm) of the exiting beam in the focal plane for different positions of the knife edge. (c): Location of the different spectral components within the beam's focal plane.

the spots or the magnitude of the shifts of the different spectral components) are attributed to slight mismatches between the alignment of the compressor and the beam (as specified in Fig. 1) and the alignment that could be achieved in the experimental setup in practice.

For further investigation, the gratings were also implemented in upside-down orientation (see Visualization 2) and in the configuration where the vertex of the period chirp is centered (see Visualization 3), by parallel shifting of the gratings. These experiments also showed high agreement with the simulation. Although they will not be further discussed in the present paper, the recorded videos, showing the cutoff of the spectral components according to the method presented in Fig. 9, are added to the supplementary material available online.

4.3. Measuring the chirp-induced lateral shift with a tunable continuous-wave laser

In order to determine the location of the pulses' spectral components within the beam in a more quantitative manner and over a broader spectral range, a wavelength-tunable continuous-wave laser was used. The experimental setup is shown in Fig. 10(a). The incident beam had a close to diffraction-limited quality and a spectrally narrow emission bandwidth of $\Delta\lambda = 0.165$ nm (FWHM) centered at a tunable wavelength. The beam was injected into the compressor through a pinhole of a white screen on which the position of the beam exiting the compressor was observed by a camera, as shown in Fig. 10(a). This observation corresponds to the analysis of the beam at plane P1 in the raytracing simulations (see Fig. 6), hence indicating lateral shifts of the beam. The approach of observing the screen with the camera instead of the direct illumination of a CCD-chip was chosen because no camera with a sufficiently large detector was available. The wavelength of the injected beam was tuned in steps of 2 nm from 1020 nm to 1040 nm.

Optics EXPRESS

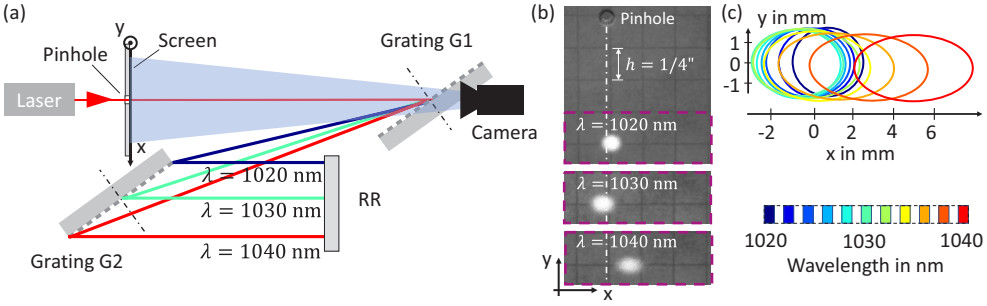

Fig. 10. (a): Simplified sketch of the setup used to directly measure the lateral displacement of the spectral components in the compressed beam. The beam of the wavelength-tunable laser is propagated through the compressor and the exiting beam is observed on the screen with a camera. (b): Three exemplary images of the beam on the screen, recorded with the camera. The pictures are mirror-inverted around the y-axis to match the perspective used in the discussion of the simulations. (c): Extracted outlines of the beam on the screen for different wavelengths of the laser.

The significant shifts of the beam on the screen observed when tuning the laser's wavelength are shown for three different wavelengths in Fig. 10(b). The pictures were mirror-inverted around the vertical axis, since the camera in the experimental setup observed the screen from the opposite side with respect to the analysis of the screen in the simulation. The recorded outlines of the cross sections of all beams (tuned from $\lambda = 1020\,\text{nm}$ to $\lambda = 1040\,\text{nm}$) on the screen are displayed in Fig. 10(c). The results show that the beam with a wavelength of $\lambda = 1030\,\text{nm}$ was centered at $x = 0$ mm, while both an increase and decrease of the wavelength led to a lateral shift to the right (positive x-direction), which is consistent with the simulations. Also as predicted by the simulation, beams with longer wavelengths were horizontally stretched while the beams with shorter wavelengths were shrunk in the horizontal direction, which is not a consequence of the beam's collimation but originates from the period chirp of the gratings. The spread of the spectral components in the vertical direction is only minor. This is consistent with the simulations (see Fig. 7), where a much smaller spread in the vertical direction was observed within plane P1 (see Fig. 7(a), indicating shifts) than in plane P2 (see Fig. 7(b), indicating tilts). Any remaining differences between the observed and the simulated spatial distribution of the spectral components are addressed to tolerances in the alignment of the gratings.

5. Discussion

The period chirp of the pulse compression gratings proved to have a detrimental effect on the beam quality and the compressibility of the compressed pulses of the investigated Treacy compressor. While this compressor was dedicated to the compression of pulses with comparatively narrow spectral bandwidth ($\Delta\lambda \approx 8\,\text{nm}$ for the experiments and $\Delta\lambda = 20\,\text{nm}$ for the simulation) and long pulse duration ($\tau \approx 500$ fs), much stronger detrimental effects are expected for the high-intensity laser systems, where spectral bandwidths of over hundred nanometers and pulse durations below a few tens of femtoseconds [55–57] are targeted. Additionally, such systems require a high contrast of the spatial and temporal intensity, where even small fractions of the peak intensity can have a detrimental influence on the targeted application [58,59]. Further simulations by us showed, that for a given system, the detrimental effects of the period chirp (defined by beam quality, angular chirp, spatial chirp, and compressibility) scale with the diameter of the incident beam, the size of the gratings, the spectral bandwidth of the pulses and the magnitude of the chirp (defined by the coefficient of the second-order term of the chirp, χ).

Optics EXPRESS

To avoid this, two strategies can be pursued. The first is to focus on the production of the gratings. When using LIL, a better collimation of the beams used for the interference is required [34] to reduce the magnitude of the chirp. Our simulations showed, that for the Treacy-Compressor investigated in this work, a period chirp of the gratings, two orders of magnitude smaller ($\chi_x = 0.22 \cdot 10^{-5}$ nm/mm^2 instead of $\chi_x = 0.22 \cdot 10^{-3}$ nm/mm^2) would have been required to maintain the beam quality and achieve the full compression of the incident pulses. Besides working on the collimation of the beams, another approach can be pursued to reduce or even eliminate the period chirp of LIL. As originally proposed by Walsh and Smith [60] and recently investigated by us [61,62], the substrate of the grating can be bent during the exposure with uncollimated beams to eliminate the period chirp. Besides LIL, also other techniques can be used for the lithographic step in the grating production. Scanning beam interference lithography (SBIL) might be a suitable alternative. Although it is more expensive, it enables the fabrication of very large gratings (up to 1 m) [63] and the precise control of the grating period [32,33]. As shown in [49], gratings fabricated by SBIL (purchased from PGL in this case) did not show any period chirp and also proved to maintain the beam quality of the pulses when employed in a compressor within our experiments and the experiments presented in [4,64].

The second strategy to limit the detrimental effects of the period chirp in compressors is to focus on the implementation of the compressor itself. To give some simple guidelines on the beneficial implementation of compressors, some additional simulations were carried out, since the results of the investigated Treacy compressor are not generally applicable to all compressor types. From these simulations, it can be stated, that (independent of the type of the compressor) the chirp is the most critical at those grating passes where the beam is large and spectrally separated. As shown in Fig. 11(a) for an in-plane four-grating compressor these are the second and the third grating passes of the beam. Due to their separation, the spectral components experience different grating periods and hence different diffraction angles. The longer the propagation distance between the second and the third grating pass, the stronger the degradation of the beam quality. For this reason, the effects of the chirp can be reduced for a Treacy compressor when the retro-reflector is positioned closer to the second grating (which contains both the 2nd and the 3rd grating pass of the beam). For in-plane four-grating compressors, as they are used in high-intensity laser systems, it is therefore recommended to implement them as shown in Fig. 11(b). Here the distances between the 2nd and the 3rd grating pass will lead to much less detrimental effects by the period chirp, compared to the much more common implementation shown in Fig. 11(a).

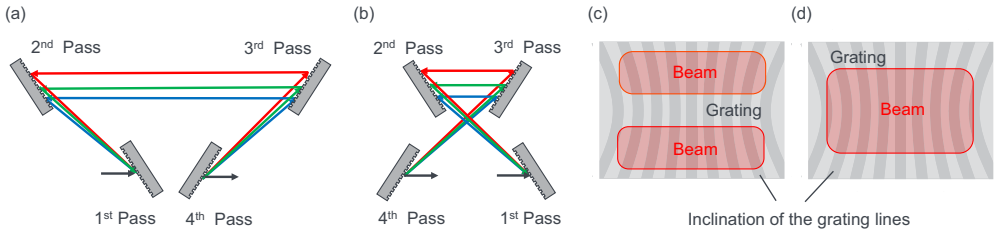

Fig. 11. Implementation of an in-plane four-grating compressor with a large (a) and a short (b) distance between the 2nd and the 3rd grating pass of the beam. Spots of the beam on one of the gratings for a Treacy-type compressor (c) and a four-grating compressor (d), indicating how the beam experiences the spatially dependent inclination of the grating lines.

Besides these similarities, there is a difference between Treacy compressors and four-grating compressors concerning the effect of the period chirp on the beam. While the beam is diffracted at two different positions on each of the two gratings within a Treacy compressor (see Fig. 1(a) and Fig. 11(c)), for four-grating compressors the beam is diffracted in the center on each of the four gratings (see Fig. 11(d)). As a consequence, the inclination of the grating lines will not lead

Optics EXPRESS

to a vertical separation of the spectral components at the output of the four-grating compressor, as it was the case for a Treacy compressor. The observed distribution of the spectral components along a c-shaped curve (see Fig. 6) will thus transform into a line where both red and blue-shifted spectral components are shifted and tilted to the right side.

Besides a change in the overall implementation of the compressors, also a change in the alignment of a given compressor could be pursued. During our experiments we also observed that a reduction of the chirp's detrimental effect can be achieved by a deliberate misalignment of the gratings. By changing the alignment and the separation of the gratings, also slightly shorter pulse durations ($\tau = 700$ fs (sech^2) at best) and better beam propagation factors ($M^2_x = 1.9$ at best) could be achieved. However, these obtained results are not in compliance with the results of the ideally aligned compressor from the simulation but represent a superposition of the adverse effects of the period chirp as well as a deliberate misalignment and will be the topic of further research.

6. Conclusion and outlook

In summary, we reported on investigations of the effects that the period chirp of pulse compression gratings has on the properties of the compressed beam of a Treacy-type compressor. Using a ray tracing simulation and different experimental setups it was shown that the period chirp introduces significant shifts and tilts of the spectral components within the beam (commonly known by the terms spatial chirp and angular chirp), which mainly result in a degradation of the beam quality and an increase in pulse duration. It was found that a characteristic spatio-spectral error pattern in the beam's intensity profile is created where the different spectral components are distributed along a c-shaped curve, both in the beam's far field and in the beam's focus. This enables the differentiation of the effects induced by the period-chirped gratings from the effects of other errors (e.g. misalignment). The three experimental approaches validated our simulative findings and hands-on methods were introduced to facilitate the unambiguous identification of the presence of a period chirp. We believe that this may provide a simple and fast method to identify potential issues with grating compressors in practice.

It is worth noting that the effects of the period chirp described in the present paper can also be found in the CPA system presented in [65]. The depicted profile of the compressed beam also shows a tail in the beam's intensity distribution and as confirmed to us by the authors, the system used a grating compressor that employed gratings fabricated by LIL.

In the future, we will pursue a theoretical and more general investigation of the effects of period chirp. This will allow us to provide a deeper understanding of the observed distribution of the different spectral components along the c-shape curve, the spectrally dependent ellipticity of the beam and the influence of the chirp on the compressor's dispersion. Also, we will investigate the option to compensate for the effects of the period chirp by deliberate misalignment of the gratings. Finally, we aim to present a simple but quantitative prediction of the detrimental effects that can be expected from specific chirped gratings for a given compressor in order to serve a much broader community of laser designers.

Funding. European Commission (687880).

Acknowledgments. This project is an initiative of the Photonics Public Private Partnership from the European Union's Horizon 2020 research and innovation programme under grant agreement No 687880.

Disclosures. The authors declare no conflicts of interest.

Data availability. Data underlying the results presented in this paper are not publicly available at this time but may be obtained from the authors upon reasonable request.

Optics EXPRESS

References

1. D. Strickland and G. Mourou, "Compression of amplified chirped optical pulses," Opt. Commun. **55**(6), 447–449 (1985).
2. S. Backus, C. G. Durfee, M. M. Murnane, *et al.*, "High power ultrafast lasers," Rev. Sci. Instrum. **69**(3), 1207–1223 (1998).
3. S. Fu, W. Zhang, W. Kong, *et al.*, "Review of pulse compression gratings for chirped pulse amplification system," Opt. Eng. **60**(2), 1–28 (2021).
4. C. Herkommer, P. Krötz, R. Jung, *et al.*, "Ultrafast thin-disk multipass amplifier with 720 mJ operating at kilohertz repetition rate for applications in atmospheric research," Opt. Express **28**(20), 30164–30173 (2020).
5. M. Müller, C. Aleshire, A. Klenke, *et al.*, "10.4 kW coherently combined ultrafast fiber laser," Opt. Lett. **45**(11), 3083–3086 (2020).
6. C. N. Danson, C. Haefner, J. Bromage, *et al.*, "Petawatt and exawatt class lasers worldwide," High Power Laser Sci. Eng. **7**, 1–54 (2019).
7. T. Tajima and G. Mourou, "Zettawatt-exawatt lasers and their applications in ultrastrong-field physics," Phys. Rev. Spec. Top. - Accel. Beams **5**(3), 031301 (2002).
8. S. Akturk, G. Xun, and R. Trebino, "Extremely simple ultrashort-pulse compressor," *Conf. Lasers Electro-Optics 2006 Quantum Electron. Laser Sci. Conf. CLEO/QELS 2006* 14, 10101–10108 (2006).
9. E. A. Gibson, D. M. Gaudiosi, H. C. Kapteyn, *et al.*, "Efficient reflection grisms for pulse compression and dispersion compensation of femtosecond pulses," Opt. Lett. **31**(22), 3363–3365 (2006).
10. C. Erny, C. Heese, M. Haag, *et al.*, "High-repetition-rate optical parametric chirped-pulse amplifier producing 1-μJ, sub-100-fs pulses in the mid-infrared," Opt. Express **17**(3), 1340–1345 (2009).
11. V. Chauhan, P. Bowlan, J. Cohen, *et al.*, "Single-diffraction-grating and grism pulse compressors," J. Opt. Soc. Am. B **27**(4), 619–624 (2010).
12. E. B. Treacy, "Optical Pulse Compression With Diffraction Gratings," IEEE J. Quantum Electron. **5**(9), 454–458 (1969).
13. G. Pretzler, A. Kasper, and K. J. Witte, "Angular chirp and tilted light pulses in CPA lasers," Appl. Phys. B **70**(1), 1–9 (2000).
14. K. Osvay, A. P. Kovács, Z. Heiner, *et al.*, "Angular dispersion and temporal change of femtosecond pulses from misaligned pulse compressors," IEEE J. Sel. Top. Quantum Electron. **10**(1), 213–220 (2004).
15. B. Webb, C. Dorrer, J. Bromage, *et al.*, "Simulation of grating compressor misalignment tolerances and mitigation strategies for chirped-pulse-amplification systems of varying bandwidths and beam sizes," Appl. Opt. **58**(2), 234–243 (2019).
16. Z. Li, T. Wang, G. Xu, *et al.*, "Research on potential problems of object image grating self-tiling for applications in large aperture optical systems," Appl. Opt. **52**(4), 718–725 (2013).
17. A. Jeandet, S. W. Jolly, A. Borot, *et al.*, "Survey of spatio-temporal couplings throughout high-power ultrashort lasers," Opt. Express **30**(3), 3262–3288 (2022).
18. Z. Li, K. Tsubakimoto, H. Yoshida, *et al.*, "Degradation of femtosecond petawatt laser beams: Spatio-temporal/spectral coupling induced by wavefront errors of compression gratings," Appl. Phys. Express **10**(10), 102702 (2017).
19. D. A. Alessi, P. A. Rosso, H. T. Nguyen, *et al.*, "Active cooling of pulse compression diffraction gratings for high energy, high average power ultrafast lasers," Opt. Express **24**(26), 30015–30023 (2016).
20. V. Leroux, S. W. Jolly, M. Schnepp, *et al.*, "Wavefront degradation of a 200 TW laser from heat-induced deformation of in-vacuum compressor gratings," *2018 Conf. Lasers Electro-Optics, CLEO 2018 - Proc.* 26, 13061–13071 (2018).
21. V. Leroux, T. Eichner, and A. R. Maier, "Description of spatio-temporal couplings from heat-induced compressor grating deformation," Opt. Express **28**(6), 8257–8265 (2020).
22. J. Qiao, J. Papa, and X. Liu, "Spatio-temporal modeling and optimization of a deformable-grating compressor for short high-energy laser pulses," Opt. Express **23**(20), 25923–25934 (2015).
23. C. Zhou, T. Seki, T. Kitamura, *et al.*, "Wavefront analysis of high-efficiency, large-scale, thin transmission gratings," *Opt. InfoBase Conf. Pap.* 22, 5995–6008 (2014).
24. Z. Li, N. Miyanaga, and L. Engineering, "Simulating ultra-intense femtosecond lasers in the 3-dimensional space-time domain," Opt. Express **26**(7), 8453–8469 (2018).
25. Z. Li and J. Kawanaka, "Complex spatiotemporal coupling distortion pre-compensation with double-compressors for an ultra-intense femtosecond laser," Opt. Express **27**(18), 25172–25186 (2019).
26. K. Osvay and I. N. Ross, "On a pulse compressor with gratings having arbitrary orientation," Opt. Commun. **105**, 271–278 (1994).
27. Z. Zhang and T. Yagi, "Evaluation of dispersion in a misaligned grating pair pulse compressor," J. Appl. Phys. **77**(2), 937–939 (1995).
28. Z. Zhong, W. Gong, H. Jiang, *et al.*, "Investigation of spatial chirp induced by misalignments in a parallel grating pair pulse stretcher," Appl. Sci. **10**(5), 1584 (2020).
29. C. Fiorini, C. Sauteret, C. Rouyer, *et al.*, "Temporal Aberrations Due to Misalignments of a Stretcher-Compressor System and Compensation," IEEE J. Quantum Electron. **30**(7), 1662–1670 (1994).
30. L. J. Guo, "Recent progress in nanoimprint technology and its applications," J. Phys. D. Appl. Phys. **37**(11), R123–R141 (2004).

Optics EXPRESS

31. Y. Chen, "Nanofabrication by electron beam lithography and its applications: A review," Microelectron. Eng. **135**, 57–72 (2015).
32. P. T. Konkola, C. G. Chen, R. K. Heilmann, *et al.*, "Nanometer-level repeatable metrology using the Nanoruler," J. Vac. Sci. Technol. B Microelectron. Nanom. Struct. **21**(6), 3097–3101 (2003).
33. C. G. Chen, P. T. Konkola, R. K. Heilmann, *et al.*, "Nanometer-accurate grating fabrication with scanning beam interference lithography," Nano- Microtechnology Mater. Process. Packag. Syst. **4936**, 126–134 (2002).
34. S. N. Dixit, J. A. Britten, R. A. Hyde, *et al.*, "Fabrication and applications of large- aperture diffractive optics," Lithogr. Micromach. Tech. Opt. Compon. Fabr. **4440**, 101–108 (2001).
35. F. Koch, D. Lehr, O. Schönbrodt, *et al.*, "Manufacturing of highly-dispersive, high-efficiency transmission gratings by laser interference lithography and dry etching," Microelectron. Eng. **191**, 60–65 (2018).
36. N. Bonod and J. Neauport, "Diffraction gratings: from principles to applications in high-intensity lasers," Adv. Opt. Photonics **8**(1), 156 (2016).
37. J. M. Carter, R. C. Fleming, T. A. Savas, *et al.*, "Interference Lithography," MTL Annual, 29–31 (2003).
38. C. P. Fucetola, H. Korre, and K. K. Berggren, "Low-cost interference lithography," J. Vac. Sci. Technol. B Microelectron. Nanom. Struct. **27**(6), 2958–2961 (2009).
39. C. J. M. Van Rijn, "Laser interference as a lithographic nanopatterning tool," J. Microlithogr. Microfabr. Microsystems **5**(1), 011012 (2006).
40. C. Lu and R. H. Lipson, "Interference lithography: A powerful tool for fabricating periodic structures," Laser Photonics Rev. **4**(4), 568–580 (2010).
41. K. Hibino and Z. S. Hegedus, "Hyperbolic holographic gratings: analysis and interferometric tests," Appl. Opt. **33**(13), 2553–2559 (1994).
42. J. Ferrera, "Analysis of distortion in interferometric lithography," J. Vac. Sci. Technol. B Microelectron. Nanom. Struct. **14**(6), 4009–4013 (1996).
43. F. Bienert, T. Graf, and M. Abdou Ahmed, "General mathematical model for the period chirp in interference lithography," Opt. Express **31**(4), 5334–5346 (2023).
44. F. Bienert, T. Graf, and M. Abdou Ahmed, "Comprehensive theoretical analysis of the period chirp in laser interference lithography," Appl. Opt. **61**(9), 2313–2326 (2022).
45. D. Weber, R. Heimburger, D. Hildebrand, *et al.*, "Use of beam-shaping optics for wafer-scaled nanopatterning in laser interference lithography," Appl. Phys. A Mater. Sci. Process. **125**(5), 307 (2019).
46. D. Virganavičius, L. Šimatonis, A. Jurkevičiūtė, *et al.*, "Formation of sub-wavelength pitch regular structures employing a motorized multiple exposure Lloyd's mirror holographic lithography setup," Proc. SPIE **9170**, 91701I (2014).
47. H. Korre, C. P. Fucetola, J. A. Johnson, *et al.*, "Development of a simple, compact, low-cost interference lithography system," J. Vac. Sci. Technol. B, Nanotechnol. Microelectron. Mater. Process. Meas. Phenom. **28**(6), C6Q20–C6Q24 (2010).
48. G. Capraro, M. Lipkin, M. Möller, *et al.*, "Phase Mask Pinholes as Spatial Filters for Laser Interference Lithography," Adv. Photonics Res. **4**(10), 1–7 (2023).
49. F. Bienert, C. Röcker, T. Graf, *et al.*, "Simple spatially resolved period measurement of chirped pulse compression gratings," Opt. Express **31**(12), 19392–19403 (2023).
50. R. Heathcote, M. Galimberti, R. J. Clarke, *et al.*, "Collimation effects on large CPA compressors," Appl. Phys. B Lasers Opt. **116**(4), 805–809 (2014).
51. X. Gu, S. Akturk, and R. Trebino, "Spatial chirp in ultrafast optics," Opt. Commun. **242**(4-6), 599–604 (2004).
52. M. Wollenhaupt, A. Assion, and T. Baumert, "Short and Ultrashort Laser Pulses," in *Springer Handbook of Lasers and Optics*, F. Träger, ed. (Springer Berlin Heidelberg, 2012), pp. 1047–1094.
53. E. Miesak and R. Negres, "Alignment Procedure for a Dual Grating Pulse Compressor," Appl. Opt. **37**(34), 8146 (1998).
54. C. Röcker, A. Loescher, M. Delaigue, *et al.*, "Flexible Sub-1 ps Ultrafast Laser Exceeding 1 kW of Output Power for High-Throughput Surface Structuring," in *Laser Congress 2019 (ASSL, LAC, LS\&C)* (Optica Publishing Group, 2019), p. AM4A.2.
55. C. Heese, C. R. Phillips, L. Gallmann, *et al.*, "Ultrabroadband, highly flexible amplifier for ultrashort midinfrared laser pulses based on aperiodically poled Mg:LiNbO3," Opt. Lett. **35**(14), 2340–2342 (2010).
56. S. Boivinet, A. Pellegrina, L. Ranc, *et al.*, "30 TW and 33 fs pulses delivered by a Ti:Sa amplifier system seeded with a frequency-doubled fiber laser," Appl. Opt. **59**(24), 7390–7395 (2020).
57. J. H. Sung, S. K. Lee, T. J. Yu, *et al.*, "0.1 Hz 1.0 PW Ti:sapphire laser," Opt. Lett. **35**(18), 3021–3023 (2010).
58. P. Mckenna, F. Lindau, O. Lundh, *et al.*, "High-intensity laser-driven proton acceleration: Influence of pulse contrast," Philos. Trans. R. Soc. A Math. Phys. Eng. Sci. **364**(1840), 711–723 (2006).
59. H. Kiriyama, A. S. Pirozhkov, M. Nishiuchi, *et al.*, "High-contrast high-intensity repetitive petawatt laser," Opt. Lett. **43**(11), 2595–2598 (2018).
60. M. E. Walsh and H. I. Smith, "Method for reducing hyperbolic phase in interference lithography," J. Vac. Sci. Technol. B Microelectron. Nanom. Struct. **19**(6), 2347–2352 (2001).
61. F. Bienert, T. Graf, and M. Abdou Ahmed, "Theoretical investigation on the elimination of the period chirp by deliberate substrate deformations," Opt. Express **30**(13), 22410–22420 (2022).

Optics EXPRESS

62. R. R. N. Rao, F. Bienert, M. Moeller, *et al.*, "Quantitative investigation on a period variation reduction method for the fabrication of large-area gratings using two-spherical-beam laser interference lithography," Opt. Express **31**(1), 371–380 (2023).
63. T. Jitsuno, S. Motokoshi, T. Okamoto, *et al.*, "Development of 91 cm size gratings and mirrors for LEFX laser system," J. Phys. Conf. Ser. **112**(3), 032002 (2008).
64. C. Herkommer, "Joule-Class Ultrafast Thin Disk Laser System with Kilohertz Repetition Rate for Atmospheric Applications," Technische Universität München (2022), page 95 pp.
65. J. Neauport, E. Lavastre, G. Razé, *et al.*, "Effect of electric field on laser induced damage threshold of multilayer dielectric gratings," Opt. Express **15**(19), 12508 (2007).